



Sunlight-driven photocatalytic oxidation of 5-hydroxymethylfurfural over a cuprous oxide-anatase heterostructure in aqueous phase

Qizhao Zhang^a, Hao Zhang^a, Bang Gu^a, Qinghu Tang^b, Qiue Cao^a, Wenhao Fang^{a,*}

^a School of Chemical Science and Technology, National Demonstration Center for Experimental Chemistry and Chemical Engineering Education, Yunnan University, 2 North Cuihu Road, 650091 Kunming, China

^b School of Chemistry and Chemical Engineering, Collaborative Innovation Center of Henan Province for Green Manufacturing of Fine Chemicals, Key Laboratory of Green Chemical Media and Reactions, Ministry of Education, Henan Normal University, 453007 Xinxiang, China

ARTICLE INFO

Keywords:

Selective oxidation
2,5-Diformylfuran
Synergistic catalysis
Holes
Singlet oxygen
Energy-band structure

ABSTRACT

Photocatalytic oxidation of 5-hydroxymethylfurfural to 2,5-diformylfuran in water is an economical and sustainable approach. We report a $(\text{Cu}_2\text{O})_x/\text{TiO}_2$ photocatalyst with p-n heterostructure by chemical reductive precipitation method. This catalyst shows $64.5 \text{ mg g}_{\text{catal}}^{-1} \text{ h}^{-1}$ of DFF production at a yield of 23% under simulated sunlight irradiation in O_2 and H_2O without any additives. It is the most outstanding result for oxide photocatalysts reported to date. We demonstrate that the content of TiO_2 determines the conversion of HMF while the content of Cu_2O and the crystalline phase of TiO_2 (i.e., anatase and rutile) impact the selectivity of DFF. The optimum strong interaction between Cu_2O and TiO_2 semiconductors is attained in the $(\text{Cu}_2\text{O})_{0.16}/\text{TiO}_2$ (anatase) photocatalyst. This not only ameliorates the pristine photoelectric property of TiO_2 but also promotes the generation of $^1\text{O}_2$ species on Cu_2O by O_2 activation. This work realizes TiO_2 -based photocatalysis with satisfactory visible-light response toward selective oxidation of HMF.

1. Introduction

Chemical conversion of renewable and abundant lignocellulosic biomass sources into sustainable fuels and chemicals has created a large consensus [1,2]. 5-Hydroxymethylfurfural (HMF) as a typical model compound for C_6 carbohydrates is recently studied for conversion of cellulose to the upgraded production of various building-block chemicals [3,4]. Of all, oxidative transformation of HMF is an important valorization route [5,6]. 2,5-Diformylfuran (DFF), the symmetrical furanic dialdehyde obtained from the selective oxidation of HMF, can serve as an essential intermediate for synthesizing diamines and Schiff bases [7,8]. Besides, DFF is viewed as an important monomer for furyl polymers, pharmaceutical intermediates, antimicrobial, etc [9,10]. As is known, the product distribution during oxidation of HMF can be complicated. Hence, the high production of DFF from HMF strongly relies on a suitable catalyst and some mild reaction conditions.

Photocatalysis enables to drive the selective oxidation of HMF to DFF under mild reaction conditions [10–14]. In that case, only room or near-room temperature and atmospheric O_2 are used. This is a promising alternative to thermal catalysis thanks to the photocatalysts with photo-generated holes and reactive oxygen species generated in the presence

of O_2 . However, very few effective catalysts have been reported in literature. Although MnO_2 nanorods [9], C_3N_4 -supported Ti_3C_2 [15], and lead-halide perovskite [16] are described as photocatalysts to give $\geq 90\%$ yield of DFF using atmospheric O_2 upon ultraviolet or visible-light irradiation, the catalytic efficiency in terms of productivity to DFF is found to reach only a moderate value ($\leq 30 \text{ mg g}_{\text{catal}}^{-1} \text{ h}^{-1}$). Notably, the complex preparation of catalysts and the compulsory use of organic solvents (i.e., nitriles and benzotrifluoride) can badly hamper the green footprint of the photocatalysis. Thereby, oxide catalysts that are low-cost, easily-prepared and readily-tunable are highly demanded. Moreover, using water instead of organic solvent as reaction medium is greener but can be much challenging for oxide catalysts. Water as a byproduct tends to block the forward reaction and water may also aggravate metal leaching. Recently, a typical Bi_2WO_6 photocatalyst was shown to afford 19% yield of DFF at a conversion of 26% using air and water and driven by visible-light [17].

Titanium dioxide (TiO_2) is regarded as one of the most common oxide photocatalysts [18–20]. TiO_2 has been extensively explored for photocatalytic degradation of organic pollutants [20–22]. However, very few applications of TiO_2 on the photocatalytic selective oxidation of biomass-derived compounds are reported, e.g., selective oxidation of

* Corresponding author.

E-mail address: wenhao.fang@ynu.edu.cn (W. Fang).

<https://doi.org/10.1016/j.apcatb.2022.122006>

Received 13 July 2022; Received in revised form 4 September 2022; Accepted 17 September 2022

Available online 19 September 2022

0926-3373/© 2022 Elsevier B.V. All rights reserved.

HMF to DFF in water phase [23–25]. Earlier, S. Yurdakal et al. prepared TiO₂ with different crystalline phases (*i.e.*, anatase, rutile, and brookite) and investigated their performances in photocatalytic oxidation of HMF to DFF in aqueous phase [23]. It was found that TiO₂ showed a strong oxidation power to quickly drive the reaction under ultraviolet irradiation at 35 °C. However, the used crystalline allotropic phases seemed not to influence the global selectivity (about 21%) of the process. The conversion could be increased but with formation of total oxidized products (*i.e.*, CO₂ and H₂O). Thereafter, to further explore the selective photo-oxidation property of TiO₂, I. Krivtsov et al. prepared nitrogen-doped and oxygen-enriched TiO₂. This N/TiO₂ catalyst may show a higher selectivity of DFF (26%) at 40% conversion of HMF at 25 °C in water using visible-light irradiation [24]. It was demonstrated that the doping of nitrogen formed Ti-O-N bonds and thus rendered the surface devoid of hydroxyl groups. This can suppress the generation of •OH radicals on TiO₂ surface and interfered the interaction of surface sites with products, thus reducing the decomposition of DFF. Recently, A. Allegri et al. prepared Au-Cu alloy particles loaded on porous TiO₂-SiO₂ nanocomposites but this Au₃Cu₁/Ti₁₅Si₈₅ photocatalyst afforded an unsatisfactory performance [25]. Only 21% conversion and 34% selectivity were obtained upon simulated sunlight irradiation at 30 °C. It was found that photogenerated holes and •OH radicals gave rise to the decomposition of HMF and its derived oxidation products.

It is clear to see for TiO₂-based photocatalysts that simultaneously tuning conversion of HMF and selectivity of DFF is critical to achieve a high yield of DFF. However, the stabilization of DFF at a high conversion of HMF remains greatly challenging. As expected, dual-functional photocatalytic systems are believed to show synergistic oxidation performance for selective formation of DFF from HMF [26]. Particularly, incorporating the extra active sites responsible for the selective conversion of an alcohol to an aldehyde to TiO₂ can be probably an effective strategy. For instance, recombining two semiconductors with different properties may often bring about unexpected results, such as formation of heterojunction or Schottky junction, which would provoke unique visible-light response or photothermal effect to a catalyst. Typically, S. Xie et al. investigated a series of traditional semiconductor catalysts for photocatalytic oxidative coupling of methanol to ethylene glycol. Interestingly, cuprous oxide (Cu₂O) was shown to be highly selective to oxidize methanol to formaldehyde under visible-light irradiation [27]. Recently, D. A. Giannakoudakis attempted a CuO_x nanoclusters (<4 nm) decorated TiO₂ photocatalyst which afforded 30% selectivity of DFF at 98% conversion of HMF but in acetonitrile under ultraviolet irradiation at 30 °C [28]. To the best of our knowledge, no efforts have been made to utilize the catalytic property of TiO₂ and Cu₂O for synergistic oxidation catalysis in aqueous phase.

Herein, this work reports a (Cu₂O)_x/TiO₂ heterojunction photocatalyst that is prepared by chemical reductive precipitation method. The strong interaction between Cu₂O and TiO₂ semiconductors enables synergistic control of the conversion of HMF and the selectivity of DFF. Hence the (Cu₂O)_x/TiO₂ catalyst attains the optimum yield and productivity of DFF in aqueous phase under simulated sunlight irradiation, in comparison with a series of typical catalysts. The prime objective is to unravel the unique photocatalytic property of the Cu₂O-TiO₂ heterostructure and then to discuss the reaction mechanism in light of the structure-activity relationship and the energy-band structure of the catalyst.

2. Experimental

2.1. Chemicals and reagents

Anatase (99.9%), rutile (99.5%), copper(II) acetate monohydrate (≥98%), glucose (99%) and Na₂CO₃ (99.8%) from Alfa Aesar, and P25 from Evonik Degussa were used for catalyst preparation. HMF (98%), DFF (98%), HMFA (98%), FFCA (98%) and FDCA (98%) from Ark Pharm were used for catalytic reactions and quantitative analysis.

2.2. Catalyst preparation

(Cu₂O)_x/TiO₂ catalysts were prepared by the chemical reductive precipitation method. Different Cu₂O/TiO₂ molar ratios (*x* = 0.08, 0.16, 0.5 and 1.5) and TiO₂ crystalline phases (anatase, rutile, as well as P25) were investigated. Unless it was specified, anatase was used as default. As an example for (Cu₂O)_{0.16}/TiO₂, copper acetate (1.4 mmol) and anatase (4.2 mmol) were mixed by 20 mL of deionized water and the mixture was ultrasonicated for 5 min. Subsequently, 20 mL of glucose solution (0.2 mol L⁻¹) was dropwise added under a magnetic stirring at 800 rpm and the mixture was stirred for 30 min. Following that, 0.2 mol L⁻¹ of Na₂CO₃ solution was added dropwise to adjust the pH to 9. Afterwards, the mixture was heated to 60 °C and aged for 2 h under stirring. The obtained solids were filtered and washed with deionized water and ethanol till the pH of filtrate reached neutral. Finally, the (Cu₂O)_{0.16}/TiO₂ catalyst was dried under vacuum at 60 °C for 12 h. Cu₂O was prepared by the same method.

2.3. Photocatalytic reactions

Typically, HMF (0.1 mmol), catalyst (30 mg) and deionized water (100 mL) were charged into a 150 mL quartz reactor, as illustrated in Scheme S1. The reaction mixture was first ultrasonicated (40 kHz) for 15 min and then stirred at dark under 500 rpm for another 15 min. This allowed a desorption equilibrium between catalyst and reactant. A Xe lamp (λ : 350–780 nm, light intensity: 0.75 W cm⁻²) CEL-HXF300-T3 from Beijing China Education Au-light Technology Co., Ltd. was used. The lamp was fixed vertically about 6 cm above the liquid surface, and the reactor was connected to a circulating water of 35 °C and an O₂ flow of 10 mL min⁻¹. Continuous sampling (0.5 mL) was done every 30 min. The quantitative analysis was conducted on an Agilent 1260 Infinity HPLC armed with a photodiode array detector and a Shodex SH-1011 sugar column (8 mm, 300 mm, 6 μ m) using a dilute H₂SO₄ solution (5 mM) as mobile phase. Specific wavelength was set for the detector, *i.e.*, 285 nm for analyzing HMF, 290 nm for DFF and FFCA, and 260 nm for HMFA and FDCA, respectively. The quantification was based on an external standard method using the standard solutions of reactant and products at different concentrations. Each reaction was performed at least twice to guarantee reliable data. Conversion of HMF, selectivity of products, yield and productivity of DFF were calculated on the basis of carbon balance.

$$\text{Conv.(\%)} = \frac{n_{\text{HMF,initial}} - n_{\text{HMF,final}}}{n_{\text{HMF,initial}}} \quad (1)$$

$$\text{Select.(\%)} = \frac{n_{\text{product}}}{n_{\text{HMF,initial}} - n_{\text{HMF,final}}} \quad (2)$$

$$\text{Yield(\%)} = \frac{n_{\text{DFF}}}{n_{\text{HMF,initial}} - n_{\text{HMF,final}}} \quad (3)$$

$$\text{Prod. (mg}_{\text{DFF}} \text{ g}_{\text{catal.}}^{-1} \text{ h}^{-1}) = \frac{W_{\text{DFF}}}{W_{\text{catal.}} \times \text{reaction time}} \quad (4)$$

2.4. Characterization methods

X-ray diffraction (XRD) analysis was performed on a Bruker D8 Advance diffractometer with Cu K α radiation and a beam voltage of 40 kV. The patterns were registered in the 2 θ domain of 10–90° at a screening rate of 0.1° s⁻¹. Transmission electron microscopy (TEM) was carried out on a field-emission JEOL-2100 F system with an acceleration voltage of 200 kV. Energy dispersive spectroscopy (EDS) elemental mapping was conducted on an X-MaxN 80 T IE250 at 200 KV. Photoluminescence spectroscopy (PL) was recorded on an Edinburgh Instruments FSL980 with 200–1700 nm steady-state spectrum. The excited wavelength was fixed at 480 nm. X-ray photoelectron spectroscopy (XPS) and Auger electron spectroscopy (AES) were carried out on a

Thermo Scientific K α system equipped with Al K α radiation under ultrahigh vacuum. The binding energy shift due to the surface charging was adjusted with a reference of the C 1 s line at 284.8 eV. Ultraviolet-visible diffuse reflectance spectrum (UV-vis DRS) was recorded on a Shimadzu UV3600 apparatus. Low-temperature electron paramagnetic resonance (EPR) spectroscopy was carried out at 100 K on a Bruker A300 EPR spectrometer with X-band frequency of 9.4 GHz. Quantitative calculation was based on the DPPH standard. Photoelectrochemical (PEC) performance of the catalyst was analyzed on an AutoLab electrochemical workstation model no. PGSTAT302N using a standard three-electrode cell. Indium tin oxide (ITO) glass deposited by the catalyst was used as the working electrode, a saturated calomel electrode (SCE) was used as the reference electrode, and a Pt wire was used as the counter electrode. To prepare the working electrode, 5 mg of catalyst was dispersed into 0.5 mL of ethanol, and then 10 μ L of Nafion® solution was added and the mixture was sonicated for 2 h to make it homogeneous. Afterwards 10 μ L of the mixed droplets were coated on the ITO glass with a controlled area of 0.25 cm², followed by drying at room temperature for 30 min to form a film electrode. The photoelectrochemical test was conducted under a 300 W xenon lamp, and a Na₂SO₄ solution (0.5 mol L⁻¹, 100 mL, pH = 6.8, 25 °C) was used as the electrolyte.

3. Results and discussion

3.1. Formation of Cu₂O||TiO₂ p-n heterojunction and synergistic photocatalytic behavior

The actual molar ratios of Cu to Ti were precisely measured by ICP-MS. The data show almost the same ratios to the theoretical values (Table S1), which reflects the effective preparation of the (Cu₂O)_x||TiO₂ catalysts by the chemical reductive precipitation method. The crystalline structure of catalyst was analyzed by XRD. As shown in Fig. 1A, well crystallized Cu₂O can be prepared from copper(II) acetate by the chemical reductive precipitation method. The characteristic diffraction peaks due to the (110), (111), (200), (220) and (311) planes of face-centered cubic Cu₂O (JCPDS #05-0667) are detected. In addition, from AES spectrum reported in Fig. S1, Cu¹⁺ ions with a typical kinetic energy at 916.5 eV are found to be the dominant species on surface [29]. For the (Cu₂O)_x||TiO₂ catalyst, Cu₂O and TiO₂ (anatase, JCPDS #21-1272) phases are clearly observed to coexist. Moreover, the intensity of Cu₂O peak apparently grows higher with increasing the Cu/Ti ratio, but the position of TiO₂ peak preserves unchanged. This indicates that Cu₂O and TiO₂ can be combined to form a mixed oxide [30]. The microstructure of the representative (Cu₂O)_{0.16}||TiO₂ catalyst was further inspected by TEM and EDS. As displayed in Fig. 1B, this catalyst shows relatively uniform nanoparticulated morphology (ca. 20 nm). EDS elemental maps present well distributed and evenly overlapped signals of Cu, Ti and O. In addition, as shown in the high-resolution TEM

image (Fig. 1C), the lattice fringe with *d* spacing of 0.234 nm and 0.350 nm can be attributed to the (111) plane of Cu₂O [31] and the (101) plane of TiO₂ [32], respectively. Notably, these crystal planes are closely contacted, which implies the formation of p-n heterojunction between Cu₂O and TiO₂ through the combination of a p-type and an n-type semiconductors.

Photocatalytic oxidation of HMF over the (Cu₂O)_x||TiO₂ catalyst was carried out under Xe lamp (λ = 350–780 nm) in aqueous phase. As shown in Fig. 2, as reference catalysts, anatase presents 100% conversion of HMF but no oxidation products are generated, whereas Cu₂O affords 100% selectivity of DFF but it is barely active. Previously, S. Yurdakal et al. disclosed that TiO₂ can effectively catalyze oxidation of HMF, but selectivity of DFF was low. They observed that CO₂ production would accumulate during the oxidation process over the lab-made TiO₂ catalysts, i.e., brookite and P25 [23]. Later, S. Xie et al. found that Cu₂O showed superior ability to selectively convert OH group to C=O groups in photo-oxidation reactions, e.g., Cu₂O was greatly selective for visible-light-driven oxidation of methanol to formaldehyde [27]. Interestingly, on the (Cu₂O)_x||TiO₂ catalyst the conversion of HMF continuously declines from 61% to 11% while the selectivity of DFF steadily goes up to 85% from 29% with increasing the Cu₂O/TiO₂ ratio from 0.08 to 1.5, as plotted in Fig. 2. Meanwhile, FFCA from over-oxidation of DFF is obtained and stabilizes at about 15% (in select.). Other products mainly including CO₂ decreases quickly and finally become zero. These results show that Cu₂O and TiO₂ can decide in synergy the performance of the (Cu₂O)_x||TiO₂ photocatalyst. As expected, a volcano-like relationship can be built between productivity of DFF and molar ratio of Cu₂O/TiO₂. The (Cu₂O)_{0.16}||TiO₂ catalyst achieves the optimal productivity of 64.5 mg g⁻¹ h⁻¹.

To understand the unique photocatalytic results, further characterizations were carried out. Usually the intensity of PL spectrum can

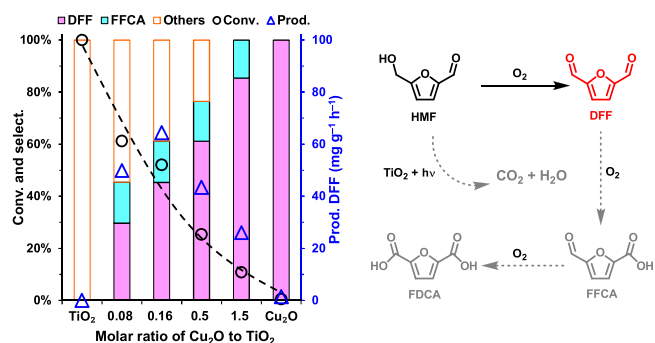


Fig. 2. Photocatalytic oxidation of HMF over TiO₂, Cu₂O and (Cu₂O)_x||TiO₂, and the main reaction pathway. Reaction conditions: HMF, 0.1 mmol; catalyst, 30 mg; H₂O, 100 mL; O₂, 10 mL min⁻¹; temperature, 35 °C; Xe lamp irradiation, 350–780 nm; time, 90 min.

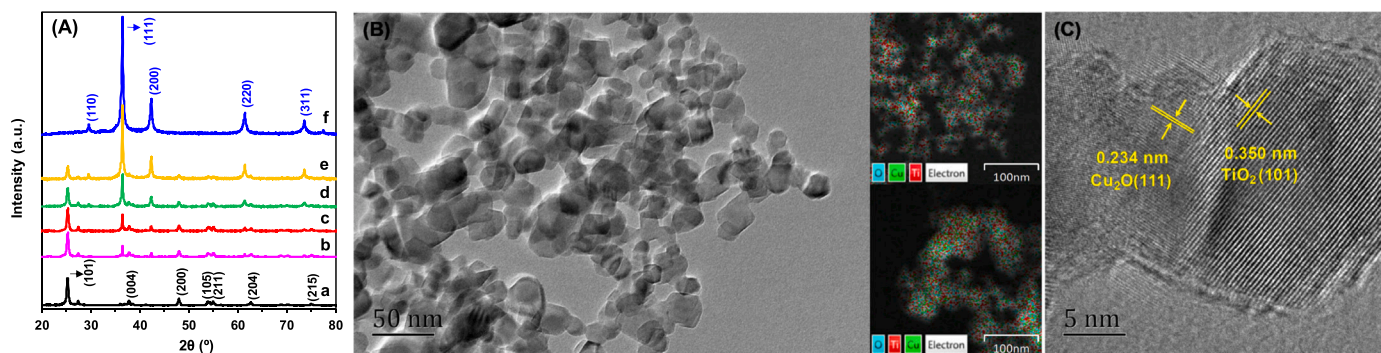


Fig. 1. (A) XRD patterns of (a) TiO₂, (b) (Cu₂O)_{0.08}||TiO₂, (c) (Cu₂O)_{0.16}||TiO₂, (d) (Cu₂O)_{0.5}||TiO₂, (e) (Cu₂O)_{1.5}||TiO₂, and (f) Cu₂O. (B) TEM image and EDS elemental maps (two areas), and (C) high-resolution TEM image with lattice-fringe marks for (Cu₂O)_{0.16}||TiO₂.

reflect the recombination efficiency of photogenerated electron-hole, and a low peak intensity indicates a low electron-hole recombination rate. As shown in Fig. 3A, TiO₂ displays the lowest fluorescence intensity in PL spectroscopy, which can correspond to the most effective separation of photogenerated electrons and holes [33]. In contrast, Cu₂O presents the highest fluorescence signal. Obviously, the formation of Cu₂O||TiO₂ heterostructure enables to modify the pristine photoelectric property of TiO₂. These results can explain the huge difference in photocatalytic activity between TiO₂ and Cu₂O for HMF conversion. Notably, the (Cu₂O)_{0.16}||TiO₂ catalyst shows the optimum separation of photogenerated electrons and holes among all the dual metal catalysts. Furthermore, photocurrent response caused by the separation and diffusion of photogenerated electron-hole pairs under light irradiation can provide some deeper information. One can see from Fig. 3B that all the catalysts show photocurrent responses but only the (Cu₂O)_{0.16}||TiO₂ catalyst apparently presents the highest value, which can reach about 1.3 and 6 folds over those of TiO₂ and Cu₂O, respectively. This unique phenomenon confirms the best separation and mobility of photogenerated electron-hole pairs on (Cu₂O)_{0.16}||TiO₂ [34], which may probably explain the highest productivity of DFF on this catalyst.

To investigate the light utilization on a photocatalyst, UV-vis DRS was performed. As displayed in Fig. 3C, TiO₂ is evidenced to show a strong absorption in UV-light region but no photoresponse in visible-light region. Interestingly, the formation of Cu₂O||TiO₂ heterojunction brings about an intense visible-light absorption. Moreover, UV-light response can be also enhanced in comparison with TiO₂ and Cu₂O. Following that, the band-gap energy (E_g) of the photocatalyst was estimated using the Tauc method by plotting $(F(R)h\nu)^{1/2}$ against $h\nu$ [24], as displayed in Fig. 3D and Table S2. When the energy of photons is equal to or greater than the band gap of a photocatalyst, electrons in the ground state can be excited and move to the high-energy level. When the absorption rapidly increases with decreasing wavelength, the corresponding energy of photons is equal to the band gap of the photocatalyst, hence electrons can move from the top of valence band to the bottom of conduction band. As shown in Fig. 3C, D, on the pristine TiO₂ and Cu₂O semiconductors, the absorption is quickly elevated from 383 and 628 nm with the corresponding band gap of 3.25 and 1.98 eV, respectively. On the (Cu₂O)_x||TiO₂ photocatalyst, one can clearly see the absorption edges of both semiconductors, in which the absorption edge of TiO₂ rises from 383 to 395 nm with increasing Cu₂O content, so that the band gap becomes relatively narrower from 3.25 to 3.15 eV. On the contrary, Cu₂O shows a decreasing absorption edge (628–610 nm) and a wider band gap (1.98–2.04 eV). It is well known that the wider the band gap is, the stronger its redox ability can be [35]. Hence, the narrower the band gap is, the stronger ability to utilize light can be obtained. Therefore, the formation of Cu₂O||TiO₂ p-n heterojunction by combining the two semiconductors is highly important for achieving a high yield of DFF via photocatalytic oxidation of HMF. That is because p-n heterojunction can enhance the light utilization ability of TiO₂ and

simultaneously improve the redox ability of Cu₂O.

Afterwards the valence states of Cu and Ti were analyzed by XPS. As shown in Fig. S2, the main peak of Cu 2p_{3/2} core level on Cu₂O can be resolved into two peaks, which can be attributed to Cu⁰/Cu¹⁺ (B.E.: 932.2 eV) and Cu²⁺ (B.E.: 933.6 eV) species [36], respectively. In the meantime, the Ti 2p core level exhibits two spin-orbit doublets due to Ti 2p_{3/2}-2p_{1/2}. Ti⁴⁺ (B.E.: 458.5 eV) as well as a very small amount of Ti³⁺ (B.E.: 457.3 eV) species can be identified for Ti 2p_{3/2} on TiO₂ [37]. With increasing Cu/Ti molar ratio in the (Cu₂O)_x||TiO₂ catalyst, the Cu peak shifts to a higher binding energy while the Ti peak shifts to a lower one (Fig. S2, Table S3). Moreover, the quantitative analyses show that the fraction of Cu⁰/Cu¹⁺ among all Cu species gently increases (75.5–80%) with increasing the Cu content, while the fraction of Ti³⁺ species accordingly decreases (9.9–7.2%). These results imply an electron transfer from Cu to Ti, and thus Cu¹⁺ species can be well stabilized on surface of the (Cu₂O)_x||TiO₂ catalyst. Importantly, the variations of HMF conversion and DFF selectivity are found to relate to the fractions of Ti³⁺ and Cu¹⁺ species, respectively.

3.2. Effect of TiO₂ crystalline phases on photocatalytic oxidation

The (Cu₂O)_{0.16}||TiO₂ catalyst prepared using different TiO₂ crystalline phases was examined by XRD. As shown in Fig. 4A, anatase (JCPDS #21–1272), rutile (JCPDS #21–1276) and P25 phases are found to be successfully combined with Cu₂O, and thus (Cu₂O)_{0.16}||TiO₂(A, R, P) heterojunctions are formed. In the time-course experiments (Fig. 4B), conversion of HMF shows similar values and trends over the (Cu₂O)_{0.16}||TiO₂ photocatalyst independent of TiO₂ crystalline phases. The conversion gradually increases from about 24% up to 64% within

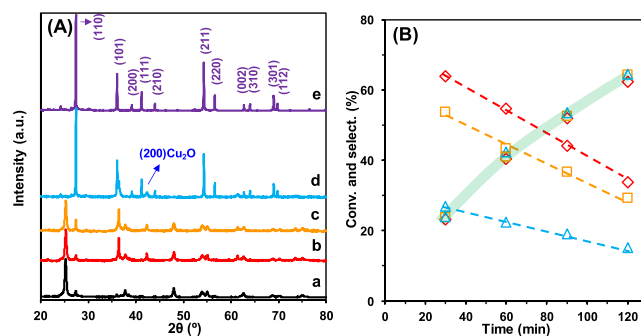


Fig. 4. (A) XRD patterns of (a) anatase, (b) (Cu₂O)_{0.16}||TiO₂(A), (c) (Cu₂O)_{0.16}||TiO₂(P), (d) (Cu₂O)_{0.16}||TiO₂(R), and (e) rutile. (B) Conversion of HMF and selectivity of DFF versus reaction time in oxidation of HMF over the (Cu₂O)_{0.16}||TiO₂(A, R, P) photocatalysts. Reaction conditions: HMF, 0.1 mmol; catalyst, 30 mg; H₂O, 100 mL; O₂, 10 mL min⁻¹; temperature, 35 °C; Xe lamp irradiation, 350–780 nm.

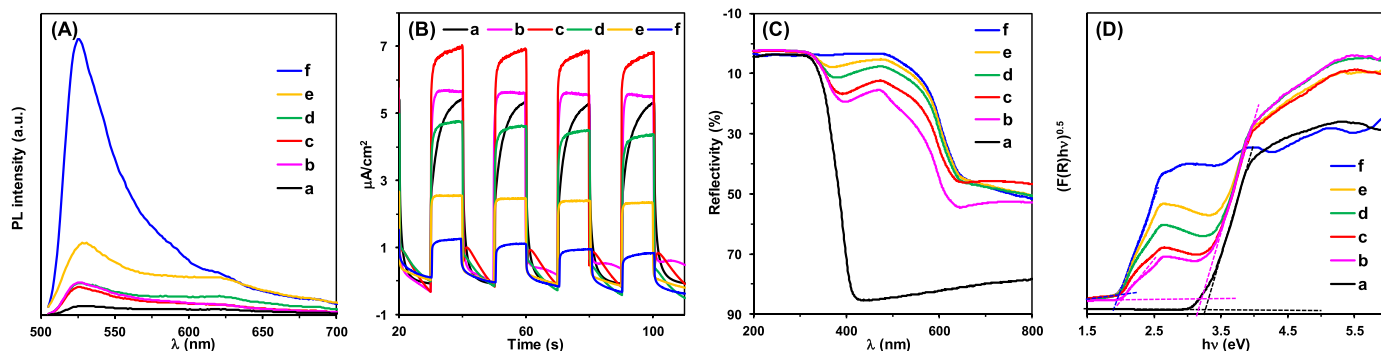


Fig. 3. (A) PL spectra, (B) photocurrent spectra, (C) UV-vis DRS, and (D) Tauc plots of (a) TiO₂, (b) (Cu₂O)_{0.08}||TiO₂, (c) (Cu₂O)_{0.16}||TiO₂, (d) (Cu₂O)_{0.5}||TiO₂, (e) (Cu₂O)_{1.5}||TiO₂, and (f) Cu₂O.

120 min. But the selectivity of DFF presents quite different values, even though the selectivity is observed to linearly decline for all the catalysts. Hence, yield of DFF first increases and then decreases, and a highest yield is obtained after 90 min over all the $(\text{Cu}_2\text{O})_{0.16}\|\text{TiO}_2(\text{A, R, P})$ catalysts (Fig. S3). Notably, the $(\text{Cu}_2\text{O})_{0.16}\|\text{TiO}_2(\text{A})$ catalyst always shows the highest selectivity of DFF during the whole reaction, which is followed by the $(\text{Cu}_2\text{O})_{0.16}\|\text{TiO}_2(\text{P})$ and $(\text{Cu}_2\text{O})_{0.16}\|\text{TiO}_2(\text{R})$ catalysts (Fig. 4B). The selectivity over $(\text{Cu}_2\text{O})_{0.16}\|\text{TiO}_2(\text{A})$ is observed to decline from 64% down to 34%. Hence the highest yield of DFF (23%) can be attained on the $(\text{Cu}_2\text{O})_{0.16}\|\text{TiO}_2(\text{A})$ catalyst. Therefore, TiO_2 crystalline phase is disclosed to significantly influence selectivity of DFF during photo-oxidation of HMF over the $(\text{Cu}_2\text{O})_{0.16}\|\text{TiO}_2$ catalyst.

To understand the interesting catalytic results, a series of characterizations and electrochemical experiments were performed to unravel the effect of TiO_2 crystalline phases. PL spectra show the emission peaks for all the $(\text{Cu}_2\text{O})_{0.16}\|\text{TiO}_2$ catalysts, which is originated from the recombination of photogenerated electrons and holes (Fig. 5A) [33]. Particularly, the $(\text{Cu}_2\text{O})_{0.16}\|\text{TiO}_2(\text{A})$ catalyst exhibits the lowest fluorescence intensity, which indicates the highest separation efficiency for photogenerated electrons and holes. Instead, $(\text{Cu}_2\text{O})_{0.16}\|\text{TiO}_2(\text{R})$ affords the lowest separation efficiency. This property was further analyzed by photoelectrochemical measurements. As shown in Fig. S4, the photocurrent generated by the $(\text{Cu}_2\text{O})_{0.16}\|\text{TiO}_2(\text{A})$ catalyst is obviously enhanced. The value can reach 1.5 and 2 folds over that of P25- and rutile-containing catalyst, respectively. These results demonstrate that anatase crystalline phase can improve generation and mobility of photogenerated electrons in the heterostructure catalyst.

In addition, electrochemical impedance spectroscopy (EIS) was used to investigate the charge-transfer rate. As expected, the semicircle Nyquist plots can be recorded in EIS for each $(\text{Cu}_2\text{O})_{0.16}\|\text{TiO}_2$ photocatalyst (Fig. 5B). For Nyquist plots, a larger diameter of the semicircle corresponds to a greater resistance to electron flow at the electrode-electrolyte interface [38]. Both anatase and Cu_2O present small and similar semicircles. After combination, the $(\text{Cu}_2\text{O})_{0.16}\|\text{TiO}_2(\text{A})$ heterojunction shows a much smaller semicircle, which can be attributed to the lowest resistance to charge transfer among all the $(\text{Cu}_2\text{O})_{0.16}\|\text{TiO}_2$ photocatalysts. Thereby, EIS confirms that anatase crystalline phase can lead to the best efficiency of electron transfer in the $(\text{Cu}_2\text{O})_{0.16}\|\text{TiO}_2$ heterostructure catalyst.

Afterwards, the surface property was deeply analyzed. As reported in Fig. S5, XPS reveals the co-presence of Ti^{4+} and Ti^{3+} ions on the surfaces of all $(\text{Cu}_2\text{O})_{0.16}\|\text{TiO}_2$ catalysts, but $(\text{Cu}_2\text{O})_{0.16}\|\text{TiO}_2(\text{A})$ presents the highest fraction of Ti^{3+} ions, followed by $(\text{Cu}_2\text{O})_{0.16}\|\text{TiO}_2(\text{P})$ and $(\text{Cu}_2\text{O})_{0.16}\|\text{TiO}_2(\text{R})$ (Table S5). AES allows precisely analyzing the valence states of surface Cu. As expected, Cu^0 , Cu^{1+} and Cu^{2+} species are simultaneously observed (Fig. 6A) [29]. However, Cu^{1+} ions are found to be dominant. The quantitative analyses find out that the $(\text{Cu}_2\text{O})_{0.16}\|\text{TiO}_2(\text{A})$ catalyst shows the highest fraction of Cu^{1+} (63.8%)

species whereas the $(\text{Cu}_2\text{O})_{0.16}\|\text{TiO}_2(\text{R})$ catalyst gives the lowest value (54.0%). In addition, typical lattice oxygen species (O^{2-}) in Ti and Cu oxides are observed while surface defective oxygen species (O^- and O_2^-) on these oxides are coexistent (Fig. 6B) [39].

The concentration of oxygen vacancies (V_O) depends on the number of lattice defects in an oxide. For Cu_2O and TiO_2 semiconductors, the amount of Cu^{2+} and Ti^{3+} ions on the heterojunction is the crucial factor to determine oxygen vacancies. As the $(\text{Cu}_2\text{O})_{0.16}\|\text{TiO}_2(\text{A})$ catalyst displays the lowest fraction of Cu^{2+} species and the highest fraction of Ti^{3+} species, the concentration of V_O sites on this catalyst ought to be situated between P25- and rutile-containing heterojunctions. EPR is a powerful technique to directly identify and measure V_O in oxides. Thereby, an in-depth inspection of V_O in the series $(\text{Cu}_2\text{O})_{0.16}\|\text{TiO}_2$ catalysts is carried out. As shown in Fig. 6C, D, the free-electron factor g is measured to be 2.004 and a signal at about 3514 G is obtained. These data have been attributed to the characteristics of V_O sites in metal oxide related to the electrophilic oxygen species (*i.e.*, O^- and O_2^-) [40]. Moreover, the quantitative analysis confirms that the $(\text{Cu}_2\text{O})_{0.16}\|\text{TiO}_2(\text{A})$ catalyst affords an intermediate concentration of V_O at 2.191×10^{17} spins g^{-1} (Fig. 6D). It is well known that V_O can act as electron donors and contribute to increase donor density over that of semiconductors [41]. It is found that $(\text{Cu}_2\text{O})_{0.16}\|\text{TiO}_2(\text{A})$ shows a suitable concentration of V_O , which is beneficial to mobility of photogenerated electrons. Thus the highest yield of DFF is attained on this catalyst.

3.3. Role of photogenerated holes and reactive oxygen species in photocatalytic oxidation

In order to unravel the role of photogenerated holes and reactive oxygen species in the optimum $(\text{Cu}_2\text{O})_{0.16}\|\text{TiO}_2(\text{A})$ catalyst for photocatalytic oxidation of HMF to DFF, some controlled experiments using scavengers were performed. The added amount of scavengers is adequate to quench the corresponding active species. Notably, a blank reaction in an atmospheric Ar implies that O_2 is the essential oxidant for the selective oxidation of HMF to DFF. Moreover, the blank tests without photocatalyst can confirm that the scavengers alone cannot drive photo-conversion of HMF in O_2 and water (Table S4). Thereby, the possible photolysis of HMF due to scavengers can be excluded. At first, sodium formate (CHOONa) and ammonium oxalate (AO) are added to the reaction, respectively. They are both regarded as reasonable scavengers for the holes in the photocatalytic system [42,43]. As shown in Fig. 7, the conversion of HMF greatly drops from 63% to 20% and 3% in the presence of sodium formate and ammonium oxalate, respectively. This phenomenon can disclose that holes play the role of oxidant for the photocatalytic conversion of HMF. And then, some typical scavengers are introduced to quench the reactive oxygen species that may be generated in the reaction. Thereby, the role of reactive oxygen species on the photocatalytic oxidation of HMF can be elucidated. As seen in Fig. 7, a significant decline in the conversion of HMF (63–6%) is observed with addition of a scavenger for singlet oxygen species ($^1\text{O}_2$), that is, 4-chloro-2-nitrophenol (4-C-2-NP) [44]. This result implies that besides the holes $^1\text{O}_2$ can be also the oxidant for conversion of HMF. In photocatalytic systems, $^1\text{O}_2$ species are usually obtained by hole oxidation of superoxide anion radicals ($\bullet\text{O}_2^-$) [45]. Hence, it can be more rational to distinguish the role of holes and $^1\text{O}_2$ species by using a scavenger of $\bullet\text{O}_2^-$ radicals, *i.e.*, *p*-benzoquinone (PBQ) [17]. It can be found that the addition of *p*-benzoquinone gives rise to dramatically decreasing the selectivity of DFF from 34% to 4%. Moreover, a blank reaction in absence of O_2 also gives highly similar results, which indicates the role of holes in TiO_2 and the generation of $\bullet\text{O}_2^-$ coming from O_2 . This clearly demonstrates that $^1\text{O}_2$ is the oxidant for selective photo-oxidation of HMF, whereas the holes exhibit strong oxidation ability and enable to destroy the furan ring in HMF molecule thus transform HMF into CO_2 and H_2O . Therefore, $\bullet\text{O}_2^-$ radical as an intermediate allow transforming the holes with strong oxidation power into $^1\text{O}_2$ species with selective oxidation ability. In photocatalytic systems,

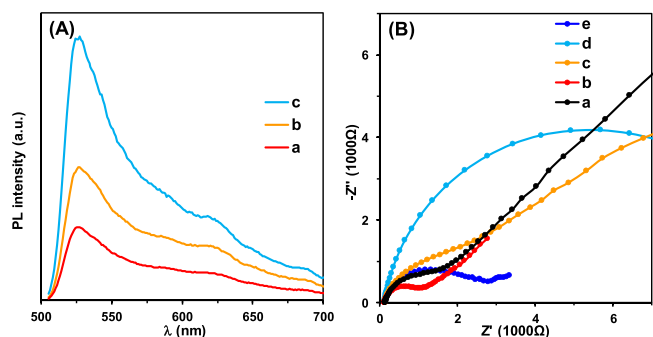


Fig. 5. PL spectra of (a) $(\text{Cu}_2\text{O})_{0.16}\|\text{TiO}_2(\text{A})$, (b) $(\text{Cu}_2\text{O})_{0.16}\|\text{TiO}_2(\text{P})$, and (c) $(\text{Cu}_2\text{O})_{0.16}\|\text{TiO}_2(\text{R})$. (B) EIS Nyquist plots of (a) anatase, (b) $(\text{Cu}_2\text{O})_{0.16}\|\text{TiO}_2(\text{A})$, (c) $(\text{Cu}_2\text{O})_{0.16}\|\text{TiO}_2(\text{P})$, (d) $(\text{Cu}_2\text{O})_{0.16}\|\text{TiO}_2(\text{R})$, and (e) Cu_2O .

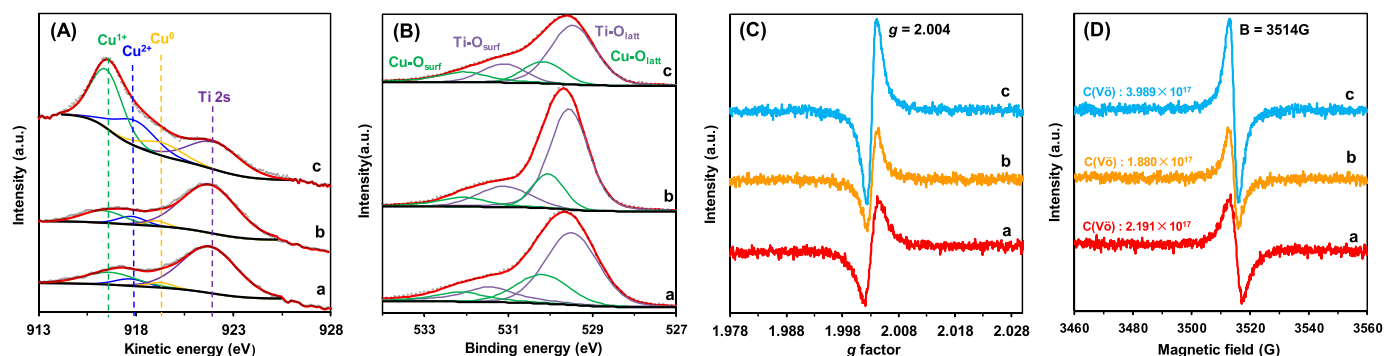


Fig. 6. (A) AES spectra of Cu LMM core level, (B) XPS spectra of O 1s core level, (C, D) low-temperature EPR spectra for (a) $(\text{Cu}_2\text{O})_{0.16}||\text{TiO}_2(\text{A})$, (b) $(\text{Cu}_2\text{O})_{0.16}||\text{TiO}_2(\text{P})$, (c) $(\text{Cu}_2\text{O})_{0.16}||\text{TiO}_2(\text{R})$, and (d) Cu_2O .

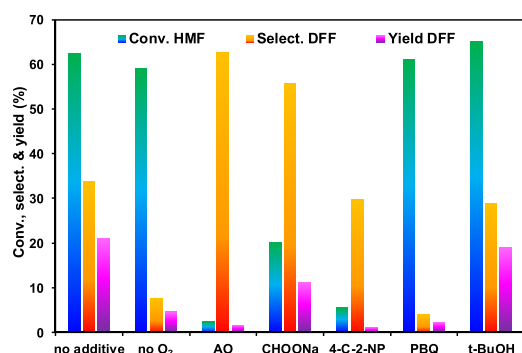


Fig. 7. Conversion of HMF, selectivity and yield of DFF during photocatalytic oxidation of HMF using the $(\text{Cu}_2\text{O})_{0.16}||\text{TiO}_2$ catalyst in the presence of different scavengers. Reaction conditions: HMF, 0.1 mmol; catalyst, 30 mg; scavenger, 5 mg; H₂O, 100 mL; O₂, 10 mL min⁻¹; temperature, 35 °C; Xe lamp irradiation, 350–780 nm; time, 120 min.

•O₂ is generally originated from the reduction of O₂ molecules by photogenerated electrons on the conduction band of a semiconductor. It has also been reported that •O₂ can be obtained by hole oxidation of H₂O to give •OH radicals, which undergo recombination and decomposition [45]. Thereby, *t*-butanol (*t*-BuOH) as the scavenger for •OH radicals is investigated [42]. It can be seen that both conversion of HMF and selectivity of DFF present a minor variation. This result reveals that the vast majority of •O₂ radicals can be generated from the reduction of O₂.

3.4. Discussion on energy-band structure and reaction mechanism

In order to understand the formation mechanism of the p-n junction, Mott Schottky (MS) plots and VB-XPS spectra of the respective catalysts were measured. MS plots were obtained from electrodes prepared with Cu₂O, $(\text{Cu}_2\text{O})_{0.16}||\text{TiO}_2(\text{A})$ and anatase. As displayed in Fig. 8A–C, $(\text{Cu}_2\text{O})_{0.16}||\text{TiO}_2(\text{A})$ and anatase exhibit n-type characteristics, while Cu₂O presents a negative-slope curve and is a p-type semiconductor [46]. The flat band potentials of Cu₂O, $(\text{Cu}_2\text{O})_{0.16}||\text{TiO}_2(\text{A})$ and anatase are determined to be 1.12, −0.25 and −0.35 V *versus* the saturated calomel electrode (SCE), respectively. It is shown for Cu₂O that the flat-band potential can be greatly affected by the surface morphology and the modification of organic ligands [47]. Therefore, the Fermi levels (E_f) of Cu₂O, $(\text{Cu}_2\text{O})_{0.16}||\text{TiO}_2(\text{A})$ and anatase are calculated to be 1.36, −0.01 and −0.11 V *versus* the normal hydrogen electrode (NHE) according to the equation $E_{\text{NHE}} = E_{\text{SCE}} + 0.2415$ V, respectively. As shown in Fig. 8D, it can be concluded that the relative energy differences (E_{VB}) of the valence band edge relative to the Fermi levels of Cu₂O and anatase are 0.39 and 2.71 eV, respectively. It is obvious to find out that the valence band signal of Cu₂O would cover that of anatase. So that the

energy difference of the valence band edge of Cu₂O in the $(\text{Cu}_2\text{O})_{0.16}||\text{TiO}_2(\text{A})$ heterojunction relative to E_f is 1.78 eV. This change can be attributed to the formation of a unified Fermi level.

As illustrated in Scheme 1, after the contact of Cu₂O with anatase, the electrons (e[−]) can transfer from the semiconductor with a higher E_f to the other semiconductor with a lower E_f [48]. It means that electrons at the donor level of anatase would migrate toward Cu₂O. Thus the electron transfer leads to movement of the Fermi level from each other and the concomitant movement of the valence band (E_{VB}) and conduction band (E_{CB}) till a uniform E_f is formed. Then the valence band edge levels (E_{VB} *versus* NHE) of Cu₂O, Cu₂O and anatase in the $(\text{Cu}_2\text{O})_{0.16}||\text{TiO}_2(\text{A})$ heterojunction, and anatase are respectively figured out to be 1.75, 1.77, 2.70 and 2.60 V, using the equation $E_{\text{VB}} = E_{\text{VB}}^0 + E_f$. And their corresponding conduction band edge levels (E_{CB} *versus* NHE) are calculated to be −0.23, −0.25, −0.49 and −0.65 V, respectively, via the equation $E_{\text{CB}} = E_{\text{VB}} - E_g$. Based on the above obtained energy band information, the formation mechanism of the $(\text{Cu}_2\text{O})_{0.16}||\text{TiO}_2(\text{A})$ heterojunction can be proposed (Scheme 1). An internal electric field directed toward Cu₂O semiconductor is generated at the interface between Cu₂O and anatase [17]. Under light irradiation, both Cu₂O and anatase are excited to simultaneously generate photogenerated electrons and holes. The internal electric field enables to accelerate the electron transfer from the conduction band of Cu₂O to the valence band of anatase. In addition, part of the holes at the valence band of anatase can be also recombined by the transferred electrons to lose the oxidation power. But the recombination rate of charge carrier in each semiconductor is significantly reduced. This leads to more electrons at the conduction band of anatase to produce •O₂, and thus more holes at the valence band of Cu₂O allow selectively oxidizing HMF to DFF.

In order to understand in-depth the effect of crystalline phases of TiO₂ in the $(\text{Cu}_2\text{O})_{0.16}||\text{TiO}_2(\text{A}, \text{R}, \text{P})$ heterojunctions on photocatalytic oxidation of HMF to DFF, all the catalysts were systematically analyzed by UV–Vis DRS (Fig. S6), MS plots (Fig. S7) and VB-XPS (Fig. S8). Moreover, HMF molecule was also measured by differential pulse voltammetry (Fig. S9) [49]. The positions of valence band and conduction band obtained by those characterizations for individual catalyst are summarized in Table S4. It can be disclosed that the potential of HMF to DFF is about 1.43 V *versus* SCE, and the potential of DFF to oxidized DFF is about 1.80 V *versus* SCE. Therefore, the potentials of HMF to DFF and DFF to oxidized DFF are calculated to be 1.67 and 2.04 V *versus* NHE. In light of the above results, the energy band structures and plausible mechanisms of electron transfer for the $(\text{Cu}_2\text{O})_{0.16}||\text{TiO}_2(\text{A}, \text{R}, \text{P})$ heterojunctions can be discussed. As illustrated in Scheme 2, the valence band position of Cu₂O is obviously more positive than the oxidation potential of HMF to DFF, but more negative than that of DFF to oxidized DFF. This demonstrates that the photo-excited holes on the valence band of Cu₂O can oxidize HMF to DFF but cannot further oxidize DFF. Instead the valence band position of TiO₂ is more negative than the oxidation potential of DFF to oxidized DFF, hence the photoexcited holes on TiO₂

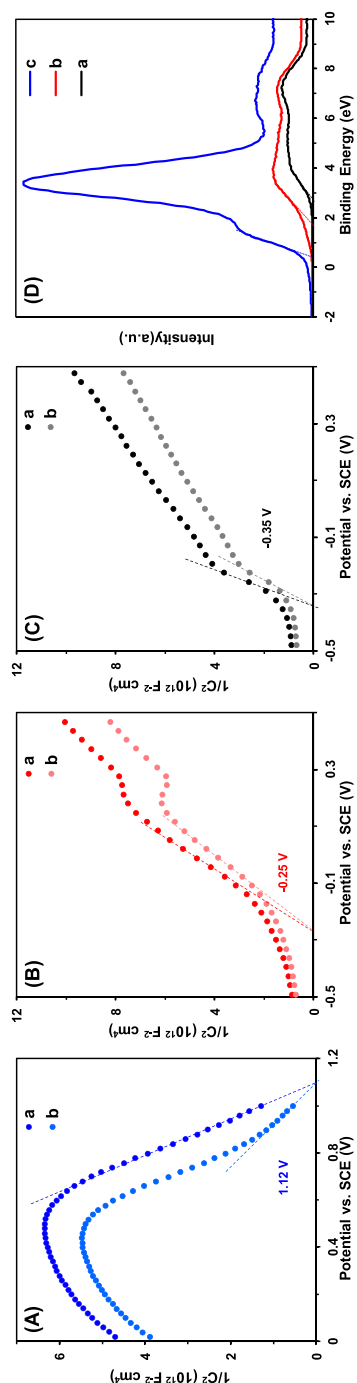
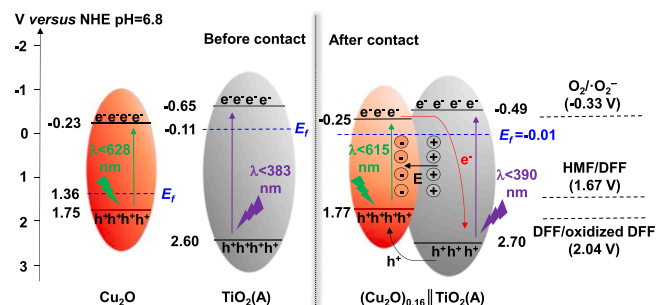


Fig. 8. Mott-Schottky plots of (A) Cu₂O, (B) (Cu₂O)_{0.16}||TiO₂(A) and (C) anatase at (a) 1000 Hz and (b) 500 Hz; (D) VB-XPS spectra of (a) anatase, (b) (Cu₂O)_{0.16}||TiO₂(A) and (c) Cu₂O.



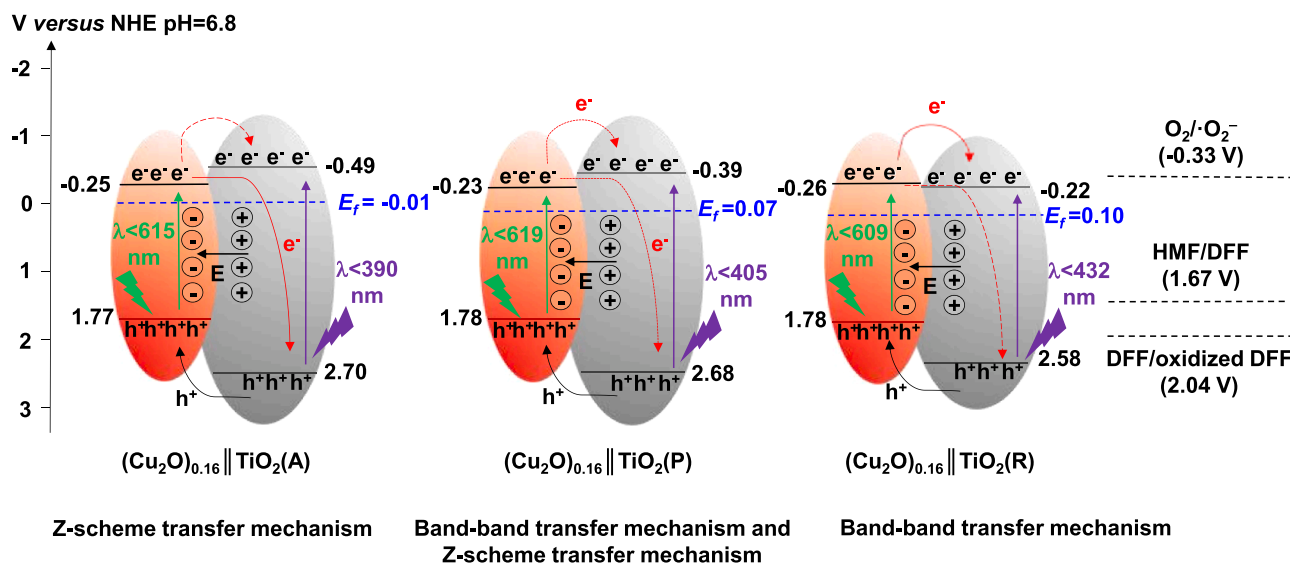
Scheme 1. Schematic illustration for energy band and charge transfer process of the Z-scheme (Cu₂O)_{0.16}||TiO₂(A).

enable to further oxidize DFF [38]. In order to realize the selective oxidation of HMF to DFF, the generation of holes at the valence band of TiO₂ must be suppressed and/or the holes can be recombined. In the (Cu₂O)_{0.16}||TiO₂(A) heterojunction catalyst, the conduction band position of anatase is found to be more negative than that of Cu₂O and the reduction potential of O₂ to •O₂. Therefore under light irradiation, photogenerated electrons at the conduction band of Cu₂O are more inclined to transfer to the valence band of anatase, which corresponds to the Z-scheme transfer mechanism [50]. At this time, part of the photogenerated holes at the valence band of anatase can be recombined by electrons and part of the holes can be transferred to the valence band of Cu₂O under the influence of electric field. As a result, the oxidation ability of anatase to further oxidize DFF can be well suppressed. On the other hand, more photogenerated electrons on the conduction band of anatase reduces O₂ to produce •O₂. •O₂ radicals are disclosed to have a good inhibitory effect on over-oxidation of DFF. Hence there are more holes in the valence band of Cu₂O, which can selectively oxidize HMF to DFF.

In the (Cu₂O)_{0.16}||TiO₂(R) heterojunction catalyst, the conduction band position of rutile is more positive than that of Cu₂O, so that the photogenerated electrons at the conduction band of Cu₂O are prone to move to the conduction band of rutile, and part of the photogenerated holes at the valence band of rutile transfer to the valence band of Cu₂O. Although there are enough electrons in the conduction band of rutile, the reduction of O₂ to •O₂ cannot spontaneously happen. That is caused by a positive position of the conduction band of rutile relative to the reduction potential of O₂ to •O₂. In this context, the band-band transfer mechanism is well adapted [50]. In comparison with anatase, there are more holes remaining on the valence band of rutile responsible for over-oxidation of DFF. As expected, the (Cu₂O)_{0.16}||TiO₂(P) catalyst can follow both transfer mechanisms. The amount of photogenerated holes at the valence band of P25 is between those of anatase and rutile, which leads to a moderate selectivity to DFF. However, the amount of holes on Cu₂O is barely unchanged whatever the mechanism. This can well explain the highly similar conversion rates obtained on the (Cu₂O)_{0.16}||TiO₂(A, R, P) heterojunction catalysts.

3.5. Light sources, catalytic stability and comparison study

Different light sources were explored on the (Cu₂O)_{0.16}||TiO₂(A) photocatalyst for selective oxidation of HMF to DFF. Light sources with different wavelengths can maintain the same strength using filters on a Xe lamp. As listed in Table 1, this catalyst shows 64% selectivity of DFF at 19% conversion of HMF under ultraviolet light (λ = 365 nm) irradiation. Whereas the catalyst behaves barely active under visible light (λ = 420–780 nm) irradiation. Only 1.5% conversion of HMF can be obtained. Notably, the (Cu₂O)_{0.16}||TiO₂(A) photocatalyst exhibits 52% conversion of HMF and 44% selectivity of DFF under Xe lamp irradiation (350–780 nm). Hence, a much higher yield to DFF (23%) is achieved in comparison with that using ultraviolet (12%) and visible (1.5%) light. These results clearly demonstrate that the unique heterostructure in



Scheme 2. Energy-band structures and plausible mechanisms of electron transfer for the $(\text{Cu}_2\text{O})_{0.16}||\text{TiO}_2(\text{A, P, R})$ heterojunctions.

Table 1

Photocatalytic oxidation of HMF over the $(\text{Cu}_2\text{O})_{0.16}||\text{TiO}_2$ catalyst under different light sources.

Light source	Conv. (%)	Select. (%)				Yield (%)	Prod. ($\text{mg g}^{-1} \text{h}^{-1}$)
		DFF	HMFA	FFCA	Others		
UV light	19	64	4	18	14	12	34.2
Vis light	1.5	100	0	0	0	1.5	4.0
Xe lamp	52	44	2	16	38	23	64.5
Sunlight ^a	12	78	7	15	0	10	26.6

Reaction conditions: HMF, 0.1 mmol; catalyst, 30 mg; H_2O , 100 mL; O_2 , 10 mL min^{-1} ; temperature, 35 °C; time, 90 min.

^a Location: 102° 42'3" east longitude and 25° 3'31" north latitude; time: 12:00–13:30; ambient atmosphere; ambient temperature.

$(\text{Cu}_2\text{O})_{0.16}||\text{TiO}_2(\text{A})$ enables to synergistically enhance the response upon ultraviolet and visible light. Such catalytic property has been evidenced by various characterizations. As expected, the $(\text{Cu}_2\text{O})_{0.16}||\text{TiO}_2(\text{A})$ heterojunction may probably catalyze the sunlight-driven photocatalytic oxidation of HMF to DFF. Indeed, this catalyst has shown an interesting result under direct sunlight irradiation and in atmosphere at city of Kunming, Yunnan province, China (Table 1). 10% yield to DFF at a selectivity of 78% can be attained. Therefore, the present $(\text{Cu}_2\text{O})_{0.16}||\text{TiO}_2(\text{A})$ photocatalyst may have potentially practical use and could realize low-cost and environmental-benign synthesis of DFF from HMF.

As important indicators for heterogeneous catalyst, the catalytic stability and reusability of the $(\text{Cu}_2\text{O})_{0.16}||\text{TiO}_2(\text{A})$ photocatalyst were examined. The used catalyst was recycled by filtration, cleaned with ethanol and deionized water, and dried at 60 °C under vacuum for 12 h. As displayed in Fig. S10, the catalyst can exhibit a stable performance during five consecutive recycling tests, showing almost unchanged conversion of HMF and selectivity of DFF. ICP-MS analysis on the post-reaction solution reveals no leaching of Cu or Ti from the catalyst during recycling tests. This can be attributed to the robust $(\text{Cu}_2\text{O})_x||\text{TiO}_2$ heterostructure. Moreover, TEM, AES and XPS were employed to analyze the catalytic property of the used catalyst. It is evident that the morphology and chemical state of the used catalyst can be well maintained in comparison with those of its fresh state (Fig. S11). This can be responsible for the superior stability and reusability of the $(\text{Cu}_2\text{O})_{0.16}||\text{TiO}_2$ catalyst.

Finally a comparison study was carried out between the $(\text{Cu}_2\text{O})_{0.16}||\text{TiO}_2(\text{A})$ catalyst and the typical metal oxide-based catalysts

reported to date in literature. As summarized in Table 2, all the benchmark catalysts can work at a low temperature (25–35 °C) in the presence of water. However, inadequate catalytic performances are usually obtained over the TiO_2 -based photocatalysts under ultraviolet and/or visible light irradiation. Either conversion of HMF ($\leq 40\%$) or selectivity of DFF ($\leq 34\%$) could only stay in a low level. Hence, yield of DFF is found to limit to 10%. Bi_2WO_6 catalyst affords a yield of 19% at 73% selectivity of DFF under visible light irradiation. It can be clearly seen that $(\text{Cu}_2\text{O})_{0.16}||\text{TiO}_2(\text{A})$ in this work exhibits the best catalytic performance. 23% yield of DFF is attained, being 2–5 folds to the TiO_2 -based catalysts and also higher than Bi_2WO_6 . Moreover, the productivity of DFF is obviously greater than all the benchmark catalysts. Therefore, the prepared $(\text{Cu}_2\text{O})_{0.16}||\text{TiO}_2(\text{A})$ heterojunction catalyst shows the most outstanding result reported in literature to date. Notably, P25- Cu_xO catalyst may offer a slightly higher yield of DFF (29%) but it requires acetonitrile as reaction solvent. Nevertheless, the productivity of DFF over this catalyst is much lower than $\text{Cu}_2\text{O}_{0.16}||\text{TiO}_2$. Interestingly, working in the presence of acetonitrile the present $\text{Cu}_2\text{O}_{0.16}||\text{TiO}_2$ catalyst shows obviously higher yield (51%) and productivity ($142.7 \text{ mg g}^{-1} \text{h}^{-1}$), more than two folds of those obtained in aqueous phase.

4. Conclusions

This work demonstrates the production of DFF from lignocellulose-derived HMF via selective oxidation in water, using a $(\text{Cu}_2\text{O})_x||\text{TiO}_2$ heterojunction photocatalyst and driven by simulated sunlight. It is disclosed that a strong interaction exists between Cu_2O and TiO_2 and the synergy between the two semiconductors determines the final catalytic performance. The formation of an internal electric field in the heterojunction can facilitate the transfer of photogenerated electrons of Cu_2O onto TiO_2 . Such process enhances the ability of Cu_2O to selectively oxidize HMF to DFF and also disables TiO_2 to oxidize HMF to CO_2 . Meanwhile, the recombination of photogenerated electrons and holes is reduced, which promotes light utilization by the $(\text{Cu}_2\text{O})_x||\text{TiO}_2$ catalyst. Moreover, it is found that the photogenerated h^+ allows oxidizing HMF to CO_2 whereas $^1\text{O}_2$ realizes the selective oxidation of HMF to DFF. In addition, it is demonstrated that the conduction-band position of anatase is more negative than that of O_2 reduction to $\bullet\text{O}_2^-$, while that of rutile is more positive. Therefore, anatase enables to reduce O_2 to produce $\bullet\text{O}_2^-$, but rutile cannot. Notably, $\bullet\text{O}_2^-$ as an intermediate plays a key role in impacting the selectivity of DFF. And this also well explains the low selectivity of DFF over rutile-containing photocatalyst.

Table 2

Comparison of catalytic performances for selective oxidation of HMF to DFF in water over oxide-based photocatalysts.

Catalyst	T (°C)	λ (nm)	Conv. HMF (%)	Select. DFF (%)	Yield (%)	Prod. (mg g ⁻¹ h ⁻¹)	Ref.
TiO ₂ (brookite)	35	365	20	21	4	53.0	[23]
N/TiO ₂	25	> 400	40	26	10	23.0	[24]
Au ₃ Cu ₁ /Ti ₁₅ Si ₈₅	30	315–1050	21	34	7	9.9	[25]
Bi ₂ WO ₆	25	> 420	26	73	19	19.2	[17]
P25-CuO _x ^a	30	365	98	30	29	12.1	[28]
(Cu ₂ O) _{0.16} TiO ₂	35	350–780	52	44	23	64.5	this work
(Cu ₂ O) _{0.16} TiO ₂ ^a	35	350–780	70	73	51	142.7	this work

^a Solvent: acetonitrile.**CRedit authorship contribution statement**

Qizhao Zhang: Conceptualization, Investigation, Methodology, Formal analysis, Writing – original draft. **Hao Zhang:** Investigation, Formal analysis. **Bang Gu:** Supervision. **Qinghu Tang:** Funding acquisition. **Qiue Cao:** Resources, Supervision. **Wenhao Fang:** Conceptualization, Resources, Supervision, Writing – review & editing, Project administration, Funding acquisition.

Declaration of Competing Interest

The authors declare that they have no known competing financial interests or personal relationships that could have appeared to influence the work reported in this paper.

Data availability

Data will be made available on request.

Acknowledgments

This work was supported by the National Natural Science Foundation of China (22272149, 22062025, 21763031), the Yunnan Fundamental Research Projects (202001AW070012, 202101AT070171), the Program for Excellent Young Talents of Yunnan University, the Yunnan University's Research Innovation Fund for Graduate Students (2021Z108), the Open Research Fund of School of Chemistry and Chemical Engineering of Henan Normal University, and the Workstation of Academician Chen Jing of Yunnan Province (202105AF150012) and the Free Exploration Fund for Academician (202205AA160007). The authors thank the Advanced Analysis and Measurement Center of Yunnan University for the sample testing service.

Author contributions

The manuscript was written through contributions of all authors. All authors have given approval to the final version of the manuscript.

Appendix A. Supplementary material

Supplementary data associated with this article can be found in the online version at [doi:10.1016/j.apcatb.2022.122006](https://doi.org/10.1016/j.apcatb.2022.122006).

References

- H.G. Cha, K.-S. Choi, Combined biomass valorization and hydrogen production in a photoelectrochemical cell, *Nat. Chem.* 7 (2015) 328–333.
- N. Luo, T. Montini, J. Zhang, P. Fornasiero, E. Fonda, T. Hou, W. Nie, J. Lu, J. Liu, M. Heggen, L. Lin, C. Ma, M. Wang, F. Fan, S. Jin, F. Wang, Visible-light-driven coproduction of diesel precursors and hydrogen from lignocellulose-derived methylfurans, *Nat. Energy* 4 (2019) 575–584.
- R.-J. van Putten, J.C. van der Waal, E. de Jong, C.B. Rasrendra, H.J. Heeres, J.G. de Vries, Hydroxymethylfurfural, a versatile platform chemical made from renewable resources, *Chem. Rev.* 113 (2013) 1499–1597.
- S. Chen, R. Wojcieszak, F. Dumeignil, E. Marceau, S. Royer, How catalysts and experimental conditions determine the selective hydroconversion of furfural and 5-hydroxymethylfurfural, *Chem. Rev.* 118 (2018) 11023–11117.
- C.R. Lhermitte, K. Sivula, Alternative oxidation reactions for solar-driven fuel production, *ACS Catal.* 9 (2019) 2007–2017.
- A. Tirsoaga, M. El Fergani, N. Nuns, P. Simon, P. Granger, V.I. Parvulescu, S. M. Coman, Multifunctional nanocomposites with non-precious metals and magnetic core for 5-HMF oxidation to FDCA, *Appl. Catal. B* 278 (2020), 119309.
- J. Xiao, X. Liu, L. Pan, C. Shi, X. Zhang, J.-J. Zou, Heterogeneous photocatalytic organic transformation reactions using conjugated polymers-based materials, *ACS Catal.* 10 (2020) 12256–12283.
- M. Zhang, Z. Yu, J. Xiong, R. Zhang, X. Liu, X. Lu, One-step hydrothermal synthesis of Cd₃In₂S₅(x+1.5y) for photocatalytic oxidation of biomass-derived 5-hydroxymethylfurfural to 2, 5-diformylfuran under ambient conditions, *Appl. Catal. B* 300 (2022), 120738.
- D.A. Giannakoudakis, V. Nair, A. Khan, E.A. Deliyanni, J.C. Colmenares, K. S. Triantafyllidis, Additive-free photo-assisted selective partial oxidation at ambient conditions of 5-hydroxymethylfurfural by manganese (IV) oxide nanorods, *Appl. Catal. B* 256 (2019), 117803.
- C. Li, J. Li, L. Qin, P. Yang, D.G. Vlachos, Recent advances in the photocatalytic conversion of biomass-derived furanic compounds, *ACS Catal.* 11 (2021) 11336–11359.
- H.-F. Ye, R. Shi, X. Yang, W.-F. Fu, Y. Chen, P-doped Zn₃Cd_{1–3}S solid solutions as photocatalysts for hydrogen evolution from water splitting coupled with photocatalytic oxidation of 5-hydroxymethylfurfural, *Appl. Catal. B* 233 (2018) 70–79.
- X. Wu, N. Luo, S. Xie, H. Zhang, Q. Zhang, F. Wang, Y. Wang, Photocatalytic transformations of lignocellulosic biomass into chemicals, *Chem. Soc. Rev.* 49 (2020) 6198–6223.
- C. Li, Y. Na, Recent advances in photocatalytic oxidation of 5-hydroxymethylfurfural, *ChemPhotoChem* 5 (2021) 502–511.
- R. Luo, Y. Li, L. Xing, N. Wang, R. Zhong, Z. Qian, C. Du, G. Yin, Y. Wang, L. Du, A dynamic Ni(OH)₂-NiOOH/NiFeP heterojunction enabling high-performance E-upgrading of hydroxymethylfurfural, *Appl. Catal. B* 311 (2022), 121357.
- X.-X. Wang, S. Meng, S. Zhang, X. Zheng, S. Chen, 2D/2D MXene/g-C₃N₄ for photocatalytic selective oxidation of 5-hydroxymethylfurfural into 2,5-formylfuran, *Catal. Commun.* 147 (2020), 106152.
- M. Zhang, Z. Li, X. Xin, J. Zhang, Y. Feng, H. Lv, Selective valorization of 5-hydroxymethylfurfural to 2,5-diformylfuran using atmospheric O₂ and MAPbBr₃ perovskite under visible light, *ACS Catal.* 10 (2020) 14793–14800.
- A. Kumar, R. Srivastava, Rose-like Bi₂WO₆ nanostructure for visible-light-assisted oxidation of lignocellulose-derived 5-hydroxymethylfurfural and vanillyl alcohol, *ACS Appl. Nano Mater.* 4 (2021) 9080–9093.
- A. Fujishima, K. Honda, Electrochemical photolysis of water at a semiconductor electrode, *Nature* 238 (1972) 37–38.
- X. Wu, J. Li, S. Xie, P. Duan, H. Zhang, J. Feng, Q. Zhang, J. Cheng, Y. Wang, Selectivity control in photocatalytic valorization of biomass-derived platform compounds by surface engineering of titanium oxide, *Chem* 6 (2020) 3038–3053.
- Y. Wang, Y. Zhang, X. Zhu, Y. Liu, Z. Wu, Fluorine-induced oxygen vacancies on TiO₂ nanosheets for photocatalytic indoor VOCs degradation, *Appl. Catal. B* 316 (2022), 121610.
- A.H. Mamaghani, F. Haghighat, C.-S. Lee, Photocatalytic oxidation technology for indoor environment air purification: the state-of-the-art, *Appl. Catal. B* 203 (2017) 247–269.
- Z. Xing, J. Zhang, J. Cui, J. Yin, T. Zhao, J. Kuang, Z. Xiu, N. Wan, W. Zhou, Recent advances in floating TiO₂-based photocatalysts for environmental application, *Appl. Catal. B* 225 (2018) 452–467.
- S. Yurdakal, B.S. Tek, O. Alagöz, V. Augugliaro, V. Loddo, G. Palmisano, L. Palmisano, Photocatalytic selective oxidation of 5-(hydroxymethyl)-2-furaldehyde to 2,5-furandicarbaldehyde in water by using anatase, rutile, and brookite TiO₂ nanoparticles, *ACS Sustain. Chem. Eng.* 1 (2013) 456–461.
- I. Krivosov, M. Ilkaeva, E. Salas-Colera, Z. Amghouz, J.R. García, E. Díaz, S. Ordóñez, S. Villar-Rodil, Consequences of nitrogen doping and oxygen enrichment on titanium local order and photocatalytic performance of TiO₂ anatase, *J. Phys. Chem. C* 121 (2017) 6770–6780.
- A. Allegri, V. Maslova, M. Blosi, A.L. Costa, S. Ortelli, F. Basile, S. Albonetti, Photocatalytic oxidation of HMF under solar irradiation: coupling of microemulsion and lyophilization to obtain innovative TiO₂-based materials, *Molecules* 25 (2020) 5225.
- W. Shang, Y. Li, H. Huang, F. Lai, M.B.J. Roelfaers, B. Weng, Synergistic redox reaction for value-added organic transformation via dual-functional photocatalytic systems, *ACS Catal.* 11 (2021) 4613–4632.

- [27] S. Xie, Z. Shen, J. Deng, P. Guo, Q. Zhang, H. Zhang, C. Ma, Z. Jiang, J. Cheng, D. Deng, Y. Wang, Visible light-driven C–H activation and C–C coupling of methanol into ethylene glycol, *Nat. Commun.* 9 (2018) 1181.
- [28] D.A. Giannakoudakis, A. Qayyum, V. Nair, A. Khan, S.R. Pradhan, J. Prekodravac, K. Rekos, A.P. LaGrow, O. Bondarchuk, D. Lomot, K.S. Triantafyllidis, J. C. Colmenares, Ultrasound-assisted decoration of CuO_x nanoclusters on TiO₂ nanoparticles for additives free photocatalytic hydrogen production and biomass valorization by selective oxidation, *Mol. Catal.* 514 (2021), 111664.
- [29] C. Peng, W. Xu, P. Wei, M. Liu, L. Guo, P. Wu, K. Zhang, Y. Cao, H. Wang, H. Yu, F. Peng, X. Yan, Manipulating photocatalytic pathway and activity of ternary Cu₂O/(001)TiO₂@Ti₃C₂T_x catalysts for H₂ evolution: effect of surface coverage, *Int. J. Hydrog. Energy* 44 (2019) 29975–29985.
- [30] T. Gao, J. Chen, W. Fang, Q. Cao, W. Su, F. Dumeignil, Ru/Mn_xCe_{1-x}O_y catalysts with enhanced oxygen mobility and strong metal-support interaction: exceptional performances in 5-hydroxymethylfurfural base-free aerobic oxidation, *J. Catal.* 368 (2018) 53–68.
- [31] G. Zhan, L. Fan, S. Zhou, X. Yang, Fabrication of integrated Cu₂O@HKUST-1@Au nanocatalysts via galvanic replacements toward alcohols oxidation application, *ACS Appl. Mater. Interfaces* 10 (2018) 35234–35243.
- [32] L. Liu, X. Gu, Y. Cao, X. Yao, L. Zhang, C. Tang, F. Gao, L. Dong, Crystal-plane effects on the catalytic properties of Au/TiO₂, *ACS Catal.* 3 (2013) 2768–2775.
- [33] M. Ilkaeva, I. Krivtsov, E.I. García-López, G. Marci, O. Khainakova, J.R. García, L. Palmisano, E. Díaz, S. Ordóñez, Selective photocatalytic oxidation of 5-hydroxymethylfurfural to 2,5-furandicarboxaldehyde by polymeric carbon nitride-hydrogen peroxide adduct, *J. Catal.* 359 (2018) 212–222.
- [34] S. Meng, X. Ye, J. Zhang, X. Fu, S. Chen, Effective use of photogenerated electrons and holes in a system: photocatalytic selective oxidation of aromatic alcohols to aldehydes and hydrogen production, *J. Catal.* 367 (2018) 159–170.
- [35] J. Ma, Z. Xiao, S. Senthilkumar, W. Zhong, Z. Shen, C. Lu, X. Jiang, X. Liu, Revealing the intrinsic nature of the synergistic effect caused by the formation of heterojunctions in Cu–Cu₂O/rGO-NH₂ nanomaterials in the catalysis of selective aerobic oxidation of benzyl alcohol, *Inorg. Chem.* 60 (2021) 14540–14543.
- [36] J. Kim, W. Choi, J.W. Park, C. Kim, M. Kim, H. Song, Branched copper oxide nanoparticles induce highly selective ethylene production by electrochemical carbon dioxide reduction, *J. Am. Chem. Soc.* 141 (2019) 6986–6994.
- [37] J. Ftouni, A. Muñoz-Murillo, A. Goryachev, J.P. Hofmann, E.J.M. Hensen, L. Lu, C. J. Kiely, P.C.A. Bruijninx, B.M. Weckhuysen, ZrO₂ is preferred over TiO₂ as support for the Ru-catalyzed hydrogenation of levulinic acid to γ -valerolactone, *ACS Catal.* 6 (2016) 5462–5472.
- [38] S. Meng, H. Wu, Y. Cui, X. Zheng, H. Wang, S. Chen, Y. Wang, X. Fu, One-step synthesis of 2D/2D–3D NiS/Zn₃In₂S₆ hierarchical structure toward solar-to-chemical energy transformation of biomass-relevant alcohols, *Appl. Catal. B* 266 (2020), 118617.
- [39] H. Zhang, T. Gao, Q. Cao, W. Fang, Tailoring the reactive oxygen species in mesoporous nio for selectivity-controlled aerobic oxidation of 5-hydroxymethylfurfural on a loaded Pt catalyst, *ACS Sustain. Chem. Eng.* 9 (2021) 6056–6067.
- [40] S. Wu, Y. Wang, Q. Cao, Q. Zhao, W. Fang, Efficient imine formation by oxidative coupling at low temperature catalyzed by high-surface-area mesoporous CeO₂ with exceptional redox property, *Chem. Eur. J.* 27 (2021) 3019–3028.
- [41] H. Tan, Z. Zhao, W.-b. Zhu, E.N. Coker, B. Li, M. Zheng, W. Yu, H. Fan, Z. Sun, Oxygen vacancy enhanced photocatalytic activity of perovskite SrTiO₃, *ACS Appl. Mater. Interfaces* 6 (2014) 19184–19190.
- [42] I. Krivtsov, E.I. García-López, G. Marci, L. Palmisano, Z. Amghouz, J.R. García, S. Ordóñez, E. Díaz, Selective photocatalytic oxidation of 5-hydroxymethyl-2-furfural to 2,5-furandicarboxaldehyde in aqueous suspension of g-C₃N₄, *Appl. Catal. B* 204 (2017) 430–439.
- [43] Y. Lu, Y. Xu, Q. Wu, H. Yu, Y. Zhao, J. Qu, M. Huo, X. Yuan, Synthesis of Cu₂O nanocrystals/TiO₂ photonic crystal composite for efficient p-nitrophenol removal, *Colloid Surf. A* 539 (2018) 291–300.
- [44] Y. Wang, Y. Xie, H. Sun, J. Xiao, H. Cao, S. Wang, Hierarchical shape-controlled mixed-valence calcium manganites for catalytic ozonation of aqueous phenolic compounds, *Catal. Sci. Technol.* 6 (2016) 2918–2929.
- [45] L. Luo, T. Zhang, M. Wang, R. Yun, X. Xiang, Recent advances in heterogeneous photo-driven oxidation of organic molecules by reactive oxygen species, *ChemSusChem* 13 (2020) 5173–5184.
- [46] J. Liu, J. Ke, D. Li, H. Sun, P. Liang, X. Duan, W. Tian, M.O. Tadé, S. Liu, S. Wang, Oxygen vacancies in shape controlled Cu₂O/reduced graphene Oxide/In₂O₃ hybrid for promoted photocatalytic water oxidation and degradation of environmental pollutants, *ACS Appl. Mater. Interfaces* 9 (2017) 11678–11688.
- [47] T.-N. Chen, J.-C. Kao, X.-Y. Zhong, S.-J. Chan, A.S. Patra, Y.-C. Lo, M.H. Huang, Facet-specific photocatalytic activity enhancement of Cu₂O polyhedra functionalized with 4-ethynylaniline resulting from band structure tuning, *ACS Cent. Sci.* 6 (2020) 984–994.
- [48] S. Meng, W. Sun, S. Zhang, X. Zheng, X. Fu, S. Chen, Insight into the transfer mechanism of photogenerated carriers for WO₃/TiO₂ heterojunction photocatalysts: is it the transfer of band–band or Z-scheme? Why? *J. Phys. Chem. C* 122 (2018) 26326–26336.
- [49] S. Radhakrishnan, K. Krishnamoorthy, C. Sekar, J. Wilson, S.J. Kim, A highly sensitive electrochemical sensor for nitrite detection based on Fe₂O₃ nanoparticles decorated reduced graphene oxide nanosheets, *Appl. Catal. B* 148–149 (2014) 22–28.
- [50] H. Li, T. Hu, R. Zhang, J. Liu, W. Hou, Preparation of solid-state Z-scheme Bi₂MoO₆/MO (MCu, Co_{3/4}, or Ni) heterojunctions with internal electric field-improved performance in photocatalysis, *Appl. Catal. B* 188 (2016) 313–323.